Meshless Deformable Models for LV Motion Analysis

Xiaoxu Wang Dimitis Metaxas
Rutgers University
110 Frelinghuysen Rd, Piscataway,
NJ, 08854, USA
xiwang@cs.rutgers.edu

Ting Chen Leon Axel
New York University
660 first Avenue, New York,
NY, 10016, USA
chent08@med.nyu.edu

Abstract

We propose a novel meshless deformable model for in vivo cardiac left ventricle (LV) 3D motion estimation. As a relatively new technology, tagged MRI (tMRI) provides a direct and noninvasive way to reveal local deformation of the myocardium, which creates a large amount of heart motion data which requiring quantitative analysis. In our study, we sample the heart motion sparsely at intersections of three sets of orthogonal tagging planes and then use a new meshless deformable model to recover the dense 3D motion of the myocardium temporally during the cardiac cycle. We compute external forces at tag intersections based on tracked local motion and redistribute the force to meshless particles throughout the myocardium. Internal constraint forces at particles are derived from local strain energy using a Moving Least Squares (MLS) method. The dense 3D motion field is then computed and updated using the Lagrange equation. The new model avoids the singularity problem of mesh-based models and is capable of tracking large deformation with high efficiency and accuracy. In particular, the model performs well even when the control points (tag intersections) are relatively sparse. We tested the performance of the meshless model on a numerical phantom, as well as in vivo heart data of healthy subjects and patients. The experimental results show that the meshless deformable model can fully recover the myocardium motion in 3D.

1. Introduction

Tagged Magnetic Resonance Imaging (tMRI) is a non-invasive way to track the *in vivo* myocardial motion during cardiac cycles. tMRI data is acquired by creating regional magnetic perturbations in the object, which are displayed in MR image as stripe-like darker tag structures embedded in relatively brighter myocardium. Tags are material properties so that they deform as the heart contracts and relaxes during the cardiac cycle. Myocardial motion in one direction can be quantitatively measured by tracking the deformation of tags that are initially in the perpendicular direction. For heart study, usually tags are created in three sets of mutually orthogonal tag planes, two of which are perpendicular to the short axis (SA) image plane and one to the long axis (LA), to form 2D tag grids in the myocardium for both views of the heart. Using appropriate mathematical approaches, we can retrieve 2D displacement fields in these image planes by tracking the deformation of tag grids. Compared to the conventional MRI which can only capture the global cardiac function measurements such as the ventricular volumes, tagged MRI can be utilized to recover local heart wall motion within the myocardium and derive potentially critical clinical information such as local torsion, shearing, and strain.

Deformable models have been widely used for the cardiac motion reconstruction from tagged MRI. Park et al. [11, 12, 13] presented deformable models combining spatially varying parameter functions to track the left ventricle (LV) motion. Haber et al. [6] and Park et al.[14, 15] further extended parameter functions to recover the right ventricle (RV) motion and conduct 4D cardiac functional analysis using Finite Element Methods (FEM). Spline models based on FEM have also been used to reconstruct the geometry of LV and RV by Declerck et al. [5] and Young [19]. Yan et al. used a Boundary Element Model (BEM) to extract local shape and motion properties of the myocardium[18]. McInerney and Terzopoulos [8] developed a FEM surface model which can track large deformation of LV. The FEM reconstructs a complex and irregular shape or motion by dividing the object mesh into a number of discrete regular shaped small elements, in which the local deformation and strain are computed using interpolation of base functions defined at mesh nodes. In general, FEM based deformable models have a good performance in recovering small and smooth local deformation. However, volumetric approaches based on FEM are vulnerable to element degeneration. When element shapes become irregular the object has to be remeshed in order to keep the motion reconstruc-

tion going. The remesh procedure is tedious and does not always guarantee returning a mesh with the optimal structure. Our volumetric model based on meshless deformable methods properly addresses this problem.

Meshfree particle methods, which are also known as meshless methods, were first introduced to deal with the modeling of objects with cracks and surface discontinuities (Belytschko et al. [1]) and have been later applied in graphical motion simulation (Muller et al. [10]). The meshless method simulates the deformation of an object by computing the motion at a set of discrete points inside the object boundary. Muller et al. [10] proposed an approach derived from continuum mechanics to simulate object deformation. Their approach used the MLS to compute the spatial derivatives of the displacement field and then used the resulting strain energy to compute the elastic forces on the point cloud representing the object of interest. Another element-free elastic model has been proposed to track the human body motion from silhouette information in Choi [4]. When the shape or the motion to be tracked is complicated, the time cost of meshless methods is usually expensive for the convergence, and they require a dense input of external forces for accurate motion tracking. We address this problem with the global deformation of deformable models.

To efficiently address the problem of large deformation tracking, we propose a new meshless deformable model which integrates parameter functions with meshless methods, i.e., the meshless method is tightly embedded into the framework of deformable models developed by Metaxas et al. [9]) as the source of internal forces. We use the new meshless model for 3D cardiac motion reconstruction from tMRI data. In the 3D motion reconstruction procedure, first we segment the heart in SA and LA images using a machine learning based method (Zhen et al. [16]), then the meshless deformable model is simultaneously registered onto SA and LA images. Intersections of tag grids are extracted from tMRI using Gabor filters to be the control points, which are the sources of external forces for the meshless deformable model. The internal forces are computed using the MLS method to simulate the elasticity of the myocardium. We compute the global deformation by calculating the parameters in local neighborhoods called phyxels and integrating over the whole volume of the myocardium. The local deformation can be recovered accurately from sparse tagged MR images using the new meshless model without being overly smoothed by interpolation. The global deformation parameters will help the model to get out of local minima during dense motion reconstruction when the tags are relatively sparse for the task.

We demonstrated the strength of the meshless deformable model as an approach for 3D cardiac motion reconstruction from tMRI by testing its performance on a numeric phantom and *in vivo* cardiac images. The experimental results showed a good convergence between our dense motion reconstruction and the underlying ground truth. Moreover, the analysis revealed the difference between normal and pathological cardiac motion.

Our paper is organized as follows: section 2 introduces the framework of the new meshless deformable model; section 3 presents the deformation results on a numerical phantom and then elaborates its medical application on tagged MRI analysis; in section 4 we draw the conclusions.

2. Meshless Deformable Models

In Metheless Deformable Models, an object under study is interpreted as particles with parameterized representation. The deformation of the object, viewed as the movement of point clouds, is reconstructed globally and locally using the Lagrange equation. In meshless methods, each particle and its neighboring particles are grouped into a phyxel with a kernel function. The global deformation of an object is described by the parameter functions and can be obtained by integrating the global motion contribution at each phyxel over the volume during a small time interval. The velocity is calculated using the Lagrange equation. The elasticity of the object is simulated by adding the internal force term, which is derived from local strain energy, into the Lagrange equation. We use a iterative framework to recursively estimate the global and local deformation in order to reconstruct the dense 3D motion in the LV myocardium.

2.1. Model Initialization

In meshless deformable models, objects are represented as the points sampled inside the object boundary.The coordinates of these points in the world coordinate system are transformed into a model-centered coordinate system, and represented as parameter functions. The transformation from the model-centered coordinate system ϕ to the world coordinate system is $x = c + Rp$, where c is the coordinates where the origin of the model-centered coordinate system is located in the world coordinate system, and R is the rotation matrix describing the orientation of ϕ. p can be further decomposed into two parts $p = s + d$, to incorporate global and local deformation.

The motion pattern shared by all particles can be described as global deformation, such as rigid transformation, scaling and twisting. We interpret s in a polar coordinate system or a cylindrical coordinate system, which has a few parameters indicating the global features of the model. Here we use the polar coordinates as our example. The model-centered coordinates of a particle e can be written in the polar coordinate (α, β, w)

$$e = wa_0 \begin{pmatrix} a_1 cos(\alpha) cos(\beta) \\ a_2 cos(\alpha) sin(\beta) \\ a_3 sin(\alpha) \end{pmatrix} \quad (1)$$

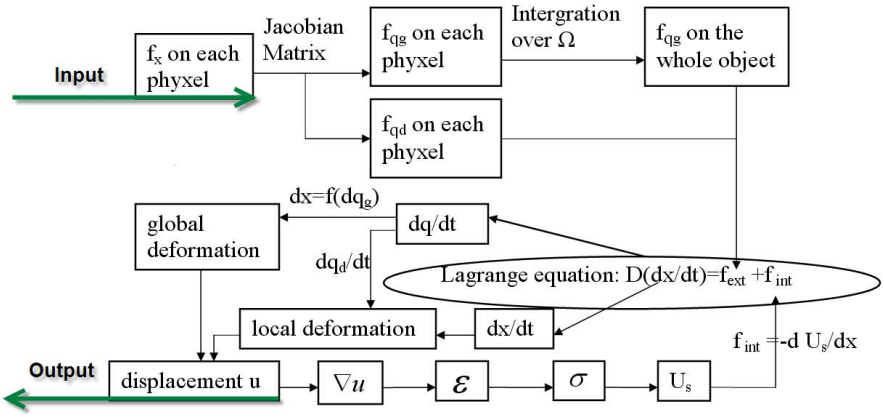

Figure 1. The flowchart of the motion reconstruction.

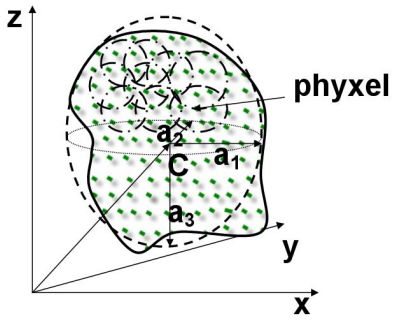

Figure 2. The meshless deformable model

where $\alpha \in [-\frac{\pi}{2}, \frac{\pi}{2}]$ varies vertically, $\beta \in [-\pi, \pi)$ varies horizontally, the transmural factor $w \in [0, 1]$ is defined in a way that it equals to 1 on model's epi-surface, and 0 at model's centroid. In the LV reconstruction, usually we define $\alpha \in [-\frac{\pi}{2}, \frac{\pi}{4}]$ runs from apex to the base of the LV. $\beta \in [-\pi, \pi)$ is horizontal, starting and ending at the inferior junction of LV and RV. Consider when there is twisting, the global deformation can be represented as $s = T(e)$:

$$s = \begin{pmatrix} e_1 cos(\varphi) - e_2 sin(\varphi) \\ e_1 sin(\varphi) + e_2 cos(\varphi) \\ e_3 \end{pmatrix} \quad (2)$$

where $\varphi = \pi\tau sin(\alpha)$. Global parameters $q_s = (a_0, a_1, a_2, a_3, \tau)$, including scale a_0, radii in three directions a_1, a_2, a_3, and a twisting factor τ. Note that the global coordinates s is a function of the point's polar coordinates (α, β, w), and the global parameters q_s:

$$s = s(q_s, (\alpha, \beta, w)) \quad (3)$$

Meshless method does not take each single particle as a unit when computing the interaction and dynamics of the particle clouds. A particle and its neighboring particles are grouped into a sphere phyxel with a kernel function. After the object deforms for a while, the shape of a phyxel may become long and narrow. When we detect ill-shaped phyxels, we can either re-sample particles or regroup particles into regular shaped phyxels based on different conditions. The mass and other values of a phyxel is distributed around each particle via the following polynomial kernel:

$$W(r, h) = \begin{cases} \frac{1}{h^9}(h^2 - r^2)^3 & \text{if } r < h \\ 0 & \text{otherwise} \end{cases} \quad (4)$$

where r is the distance to the center particle and h is the current support radius of the kernel. The kernel is normalized by dividing by constant $\int_x W(|x - x_0|, h)dx$. During the motion estimation, for each particle i we compute the average distance $\bar{r}_i$ to its 10 nearest neighbors and set the $h = 3\bar{r}_i$. The value of h for each phyxel updates every five iterations in motion estimation. The neighborhood of a particle is computed and stored in a hash table to speed up the motion reconstruction [17].

2.2. Lagrangian Dynamics

Considering the deformation potential energy functional $\mathcal{E}(x)$ and the (Rayleigh) dissipation functional $\mathcal{F}(x) = \frac{1}{2}\int_\Omega \gamma|\dot{x}|^2$, the Lagrangian equation for the model is

$$\frac{\partial \mathcal{F}(x)}{\partial \dot{x}} + \delta_x \mathcal{E} = f_{ext} \quad (5)$$

recall the definition of x as the displacement of a structure, $\dot{x}$ is the velocity, and f_{ext} is the external force. By defining the damping matrix $\mathbf{D}$ and the internal force $f_{int} = -\delta_x \mathcal{E}$ The equation can be rewritten as

$$\mathbf{D}\dot{x} = f_{ext} + f_{int} \quad (6)$$

In this paper we define the damping matrix $\mathbf{D}$ be diagonal and constant over time. The internal force is only considered in local deformation.

The velocity of a point in world coordinates can be calculated as

$$\begin{aligned} \dot{x} &= \dot{c} + \dot{\mathbf{R}}p + \mathbf{R}\dot{p} \\ &= \dot{c} + \mathbf{B}\dot{\theta} + \mathbf{R}\dot{s} + \mathbf{R}\dot{d} \end{aligned} \tag{7}$$

where $\mathbf{B} = \partial(\mathbf{R}p)/\partial\theta_i$ and $\dot{s} = [\partial s/\partial q_s]\dot{q_s} = J\dot{q_s}$. J is the Jacobian of the model-centered coordinates with respect to the global deformation parameters at each phixel. In the model expressed in equation (1) and (2), $\partial s/\partial q_s = (\partial s/\partial a, \partial s/\partial \tau) = ((\partial s/\partial e)(\partial e/\partial a), \partial s/\partial \tau)$, where $a = (a_0, a_1, a_2, a_3)$.

Equation 7 can be written in the form

$$\dot{x} = [\mathbf{I}\ \mathbf{B}\ \mathbf{RJ}\ \mathbf{R}]\dot{q} = \mathbf{L}\dot{q} \tag{8}$$

where $\mathbf{J} = (J_1, ..., J_n)$, $q = (c, \theta, s, d)$, and n is the number of points in the object. We can omit the local deformation d in the stimation of global parameters so that the velocity of the global variables $q_g = (c, \theta, s)$ can be calculated by combining formula 6 and formula 8.

$$\dot{q_g} = f_{q_g} = \int_\Omega f_{ext}\mathbf{L} \tag{9}$$

The external forces f_{ext} on global parameters are integrated over the volume

$$f_{q_g} = \int_\Omega f_{ext}\mathbf{L} = (f_c, f_\theta, f_s) \tag{10}$$

where

$$f_c = \int_\Omega f_{ext} \tag{11}$$

$$f_\theta = \int_\Omega f_{ext}\mathbf{B} \tag{12}$$

$$f_s = \int_\Omega f_{ext}\mathbf{RJ} \tag{13}$$

The integration over the volume can be interpreted as the sum of the integrals over each phyxel in the volume. The integration of f in the phyxel centered at point x_0 is

$$\int_{phyxel} f dx = \sum_x f_x W(|x - x_0|, h) \tag{14}$$

The weights of particles in phyxels are pre-computed during each initialization procedure and saved for later use.

Replacing the velocity in the Lagrangian equation (6) with the velocity of parameters in equation (8), we can update the parameters using an explicit iterative scheme

$$q_{t+1} = q_t + (f_q)dt \tag{15}$$

2.3. Meshless Methods

The internal forces are calculated by meshless methods as the derivatives of the strain energy, which is computed from strain and stress. To compute strain, the deformation gradient is computed per phyxel with MLS (Lancaster and Salkauskas [7]). MLS minimized the weighted difference between the observed displacement of a particle and the displacement approximated by its neighbors with first order accuracy

$$e = \sum_j (\tilde{u}_j - u_j)^2 w_{ij}, \text{ where } \tilde{u}_j = u_i + x_{ij}^T \nabla u|_{x_i} \tag{16}$$

Components of the displacement gradient ∇u at node i can be computed as (for example, the x component):

$$\begin{aligned} \nabla u_x|_i = A^{(-1)} \textstyle\sum_j (u_x(j) - u_x(i)) x_{ij} w_{ij}, \\ \text{where } A = \textstyle\sum_j x_{ij} x_{ij}^T w_{ij} \end{aligned} \tag{17}$$

There are more points within the support radius of a kernel than in one element of FEM, and points inside a kernel are predefined not to be co-planar or co-linear, so that the possibility that A in equation (17) is singular can be neglected.

Given the initial position of a phyxel $x_0 = (x, y, z)$ in a world coordinate and the displacement $u(t) = (u_x, u_y, u_z)$ at time t, the current position of the phyxel in the deformed model is $x(t) = x_0 + u(t)$. The Jacobian of this mapping is

$$J = I + \nabla u^T = \begin{bmatrix} 1 + u_{x,x} & u_{x,y} & u_{x,z} \\ u_{y,x} & 1 + u_{y,y} & u_{y,z} \\ u_{z,x} & u_{z,y} & 1 + u_{z,z} \end{bmatrix} \tag{18}$$

Given the Jacobian J, the Lagrangian strain tensor ε of the phyxel is

$$\varepsilon = (J^T J - I) = \nabla u + \nabla u^T + \nabla u \nabla u^T \tag{19}$$

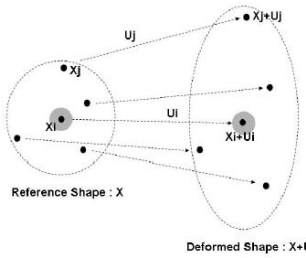

Figure 3. The deformation of a phyxel

The stress σ depends on the strain ε as

$$\sigma = C\varepsilon \tag{20}$$

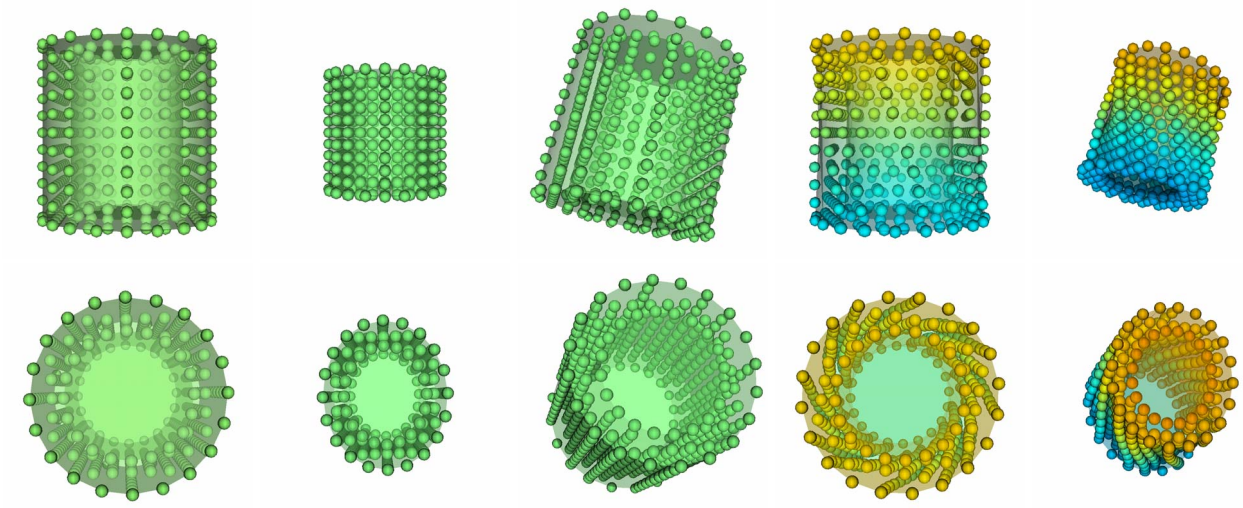

Figure 4. Deformation on phantom(from left to right): initial, scaling, rotation, twisting, combination of three deformation.

where C is a rank six matrix containing the Young's modulus and Poisson ratio for material property control.

The strain energy stored around phyxel i can be computed as

$$U_i = v_i \frac{1}{2}(\varepsilon_i \cdot \sigma_i) \tag{21}$$

where v_i is the volume of the phyxel.

The force on particle j, which is caused by the deformation of phyxel i, can be computed as the derivative of the strain energy

$$f_j = -\nabla_{u_j} U_i = -v_i \sigma_i \nabla_{u_j} \varepsilon_i \tag{22}$$

The internal force on point i is the negative sum of all f_j of its neighbors j.

$$f_{int,i} = -\sum_j f_j \tag{23}$$

3. Experimental Results

3.1. Test on Phantom

We test the meshless deformable model with a numeric phantom. The results are displayed in Figure 4. Particles are sampled between two nested cylinders (the phantom). We draw external forces from the corresponding locations of control points in the template and the target. To test the performance of the meshless model with sparse sampling, we reconstruct the motion several times using different proportions of the control points. Our results show that the model can reconstruct dense motion field with scaling, rotation, twisting, and the combination of all three. Using the phantom with a radius of 15 millimeters (mm) and a height of 30 mm, the model fits the ground truth with discrepancy less than 0.1 mm within 5 seconds. The model converges to the target even when we only use part of the control points. Figure 5 displays the number of iterations versus the proportion of control points we use for the reconstruction. The blue line shows the average number of iterations taken to achieve the same accuracy threshold in motion reconstruction. It takes about 40 iterations when all sample points are used as control points and the model can still converge to the same accuracy level using 10% of all control points within 160 iterations. This feature enables the model to track deformation when control points are relatively sparse, which is common for tMRI data.

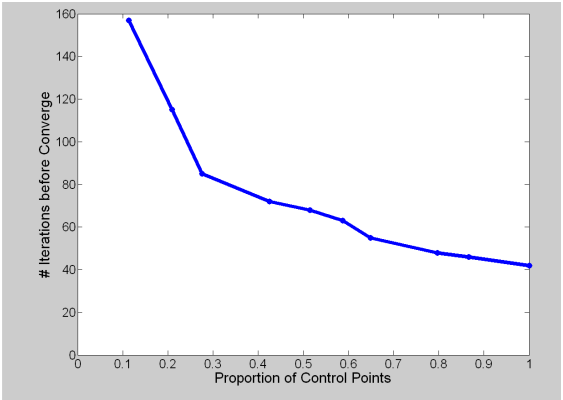

Figure 5. The number of iterations versus the proportion of control points.

3.2. Reconstruction of Cardiac Motion

Tagged MR images were obtained from a Siemens Trio 3T MR scanner with 2D grid tagging. The 3D tagged MR image set we used consisted of a stack of 8 SA image sequence equally spaced from the base to the apex of LV, and

3 LA images which are parallel to the long axis (LA) and with 60 degree angles in between, as shown in Figure 6

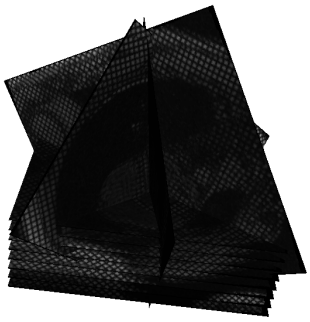

Figure 6. The setting of MRImages: 8 SA parallel images are placed with equally space from apex to base. 3 rotated LA images are taken with 60 degree angles in between.

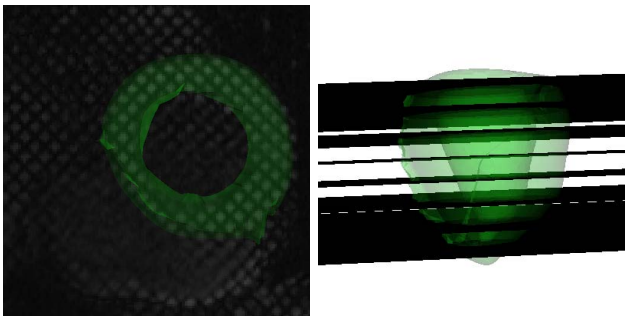

Figure 7. Registered LV on SA images

To register the model with the image data, we detected a set of landmarks, 50 per SA slice and 400 in total, on the myocardial contours based on local curvature. The landmarks were then matched between image contours and the corresponding slices of the model. The matched point pairs provided long range external forces for the convergence of the meshless deformable model and the image data. The LA and SA were previously registered using rigid registration based on the spatial information in the dicom header file. The boundary of the registered heart is displayed in Figure 7.

The automatic tracking of tag intersections was critical in preprocessing since it provided the external forces on the control points in the meshless deformable model. As introduced in Chen et al. [2, 3], a Gabor filters bank was implemented to generate corresponding phase maps for tMRI images. A Robust Point Matching (RPM) module has been integrated into the approach to avoid false tracking results caused by through-plane motion and irregular tag spacing. Tracked tag intersections are shown in Figure 8.

We reconstructed the motion of a normal heart (Figure 9) and a hypertrophied heart (Figure 10). The heart motion in a cardiac cycle is complicated. To simplify the display,

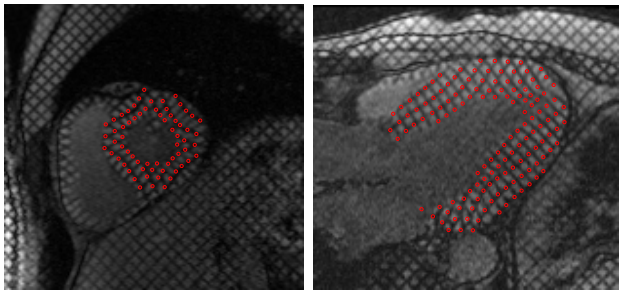

Figure 8. The intersections of grid tagging lines tracked by gabor filters

3D motions are decomposed into three components corresponding to LA, radial and circumferential directions (Figure 9). Figure 9 (b), the largest movement of the LV we observed is the shortening along the LA direction. The centroid of the LV moves toward the apex during the systole. Figure 9 (c), the magnitude of radial contraction in the free wall is larger than the radial contraction in the septum. The twisting of the LV is displayed in Figure 9 (d). The upper half of the LV from base to middle rotates clockwise and the lower half of the LV from apex to middle rotates counter clockwise.

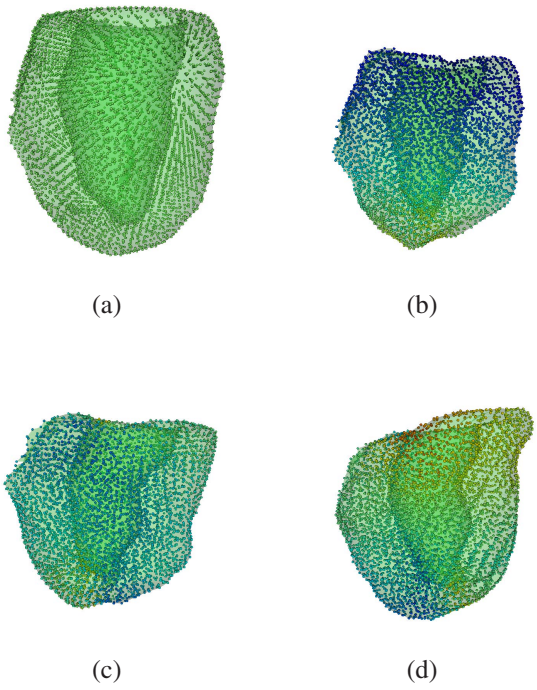

Figure 9. (a) The LV of a normal heart at the end of diastole is take as the initial state; (b)(c)(d) are the LV of a normal heart at the end of systole. (b) shows the displacements along long axis; (c) shows the displacements in radial direction; (d) shows the displacements in circumferential direction.

The hypertrophic heart has thicker wall. The motion magnitude of the hypertrophic heart is smaller than that of a

normal heart. The contraction and relaxation of the hypertrophic heart takes longer time in a cardiac cycle as shown in Figure 11 - 16. We denote the distance from the model center to the apex as the LA radius in this paper. The length unit is set to millimeters; the angle unit is set to degrees; and the time axis is proportional to one cardiac cycle.

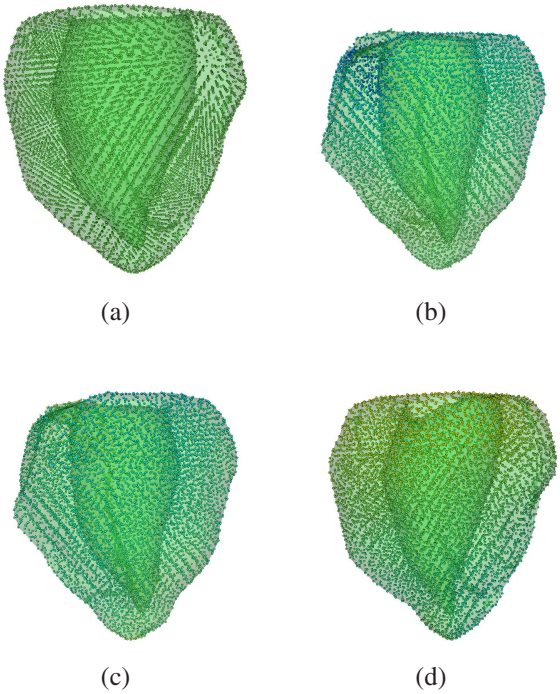

Figure 10. (a) The LV of a hypertrophied heart at end diastole is taken as the initial state; (b)(c)(d) are the LV of a hypertrophied heart at end systole. (b) shows the displacements along long axis; (c) shows the displacements in radial direction; (d) shows the displacements in circumferential direction.

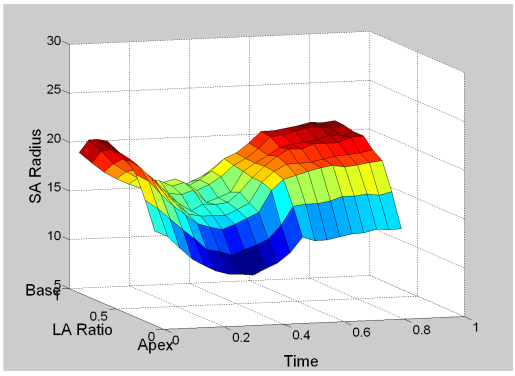

Figure 11. Average radius in SA from apex to base in a normal heart beating cycle

4. Conclusions and Discussion

We have presented a new meshless deformable model for tracking of the complex 3D motion of myocardium. Our model can track the translation, rotation, scaling, twisting, and local deformation simultaneously. The model avoids time consuming remeshing procedure by simulating the volume with particles and phyxels. The comparison between our results and the ground truth of the numerical phantom demonstrated the robust motion reconstruction performance of the model, even with sparse external forces. The experiments on *in vivo* tMRI data prove the strength of the model against motion complexity, image artifacts, and noises. The

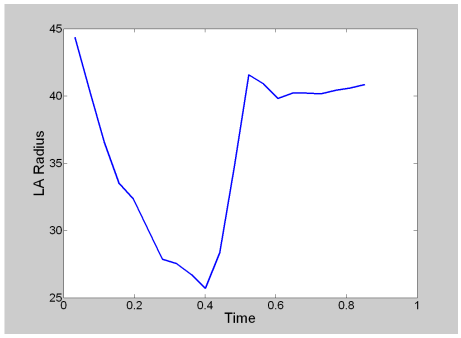

Figure 12. Long Axis motion in a normal heart beating cycle

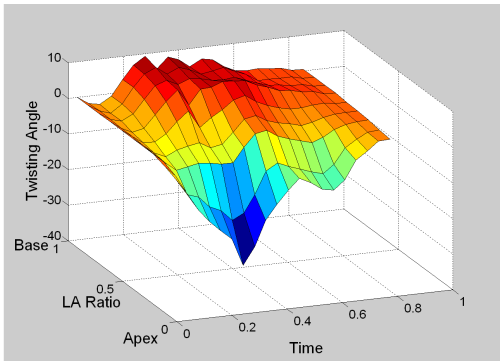

Figure 13. Twisting angles from apex to base in a normal cardiac cycle

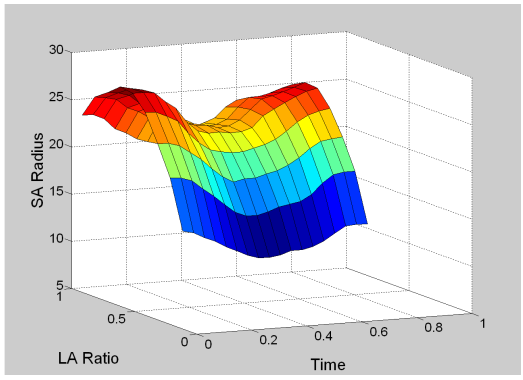

Figure 14. Average radius in SA from apex to base in a hypertrophied cardiac cycle

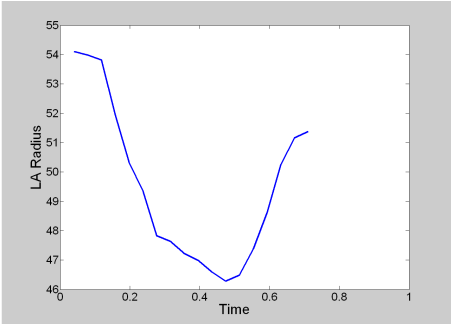

Figure 15. Long Axis motion in a hypertrophied cardiac cycle

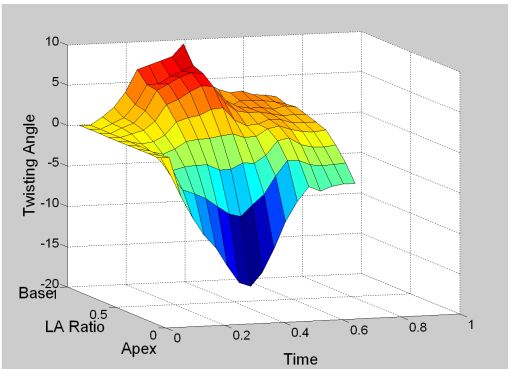

Figure 16. Twisting angles from apex to base in a hypertrophied cardiac cycle

new meshless model is time efficient compared to conventional meshless methods. In the future we are going to systematically validate the 3D cardiac motion reconstruction from tMRI.

References

[1] T. Belytschko, Y. Krongauz, D. Organ, M. Fleming, and P. Krysl. Meshless methods: An overview and recent developments. *Computer Methods in Applied Mechanics and Engineering*, pages 3–47, 1996. 2

[2] T. Chen, S. Chung, and L. Axel. 2d motion analysis of long axis cardiac tagged mri. *Proceedings of Medical Image Computing and Computer-Assisted Intervention*, pages 469–476, 2007. 6

[3] T. Chen, S. Chung, and L. Axel. Automated tag tracking using gabor filter bank, robust point matching, and deformable models. *Proceedings of Functional Imaging and Modeling of the Heart*, pages 22–31, 2007. 6

[4] J. Choi, A. Szymczak, G. Turk, and I. Essa. Element-free elastic models for volume fitting and capture. *Proceedings of Computer Vision and Pattern Recognition*, pages 2245–2252, 2005. 2

[5] J. Declerck, J. Feldmar, and N. Ayache. Definition of a 4d continuous planispheric transformatin for the tracking and the analysis of the LV motion. *Medical Image Analysis*, pages 197–213, 1998. 1

[6] E. Haber, D. N. Metaxas, and L. Axel. Motion analysis of the right ventricle from the mri images. *Proceedings of Medical Image Computing and Computer-Assisted Intervention*, pages 177–188, 1998. 1

[7] P. Lancaster and K. Salkauskas. Surfaces generated by moving least squares methods. *Mathematics of Computation*, pages 141–158, 1981. 4

[8] T. McInerney and D. Terzopoulos. A dynamic finite element surface model for segmentation and tracking in multidimensional medical images with application to cardiac 4d image analysis. *Computerized Medical Imaging and Graphics*, 19(1):69–83, 1995. 1

[9] D. N. Metaxas and D. Terzopoulos. Dynamic 3D models with local and global deformations: Deformable superquadrics. *IEEE Transaction on Pattern Analysis Machine Intelligence*, 13(7):703–714, 1991. 2

[10] M. M'uller, R. Keiser, A. Nealen, M. Pauly, M. Gross, and M. Alexa. Point based animation of elastic, plastic and melting objects. *Proceedings of the 2004 ACM SIGGRAPH/Eurographics symposium on Computer animation*, pages 141–151, 2004. 2

[11] J. Park, D. Metaxas, and L. Axel. Volumetric deformable models with parameter functions: A new approach to the 3D motion analysis of the LV from MRI-SPAMM. In *ICCV*, pages 700–705, 1995. 1

[12] J. Park, D. Metaxas, and L. Axel. Deformable models with parameter functions for cardiac motion analysis. In *IEEE Transactions on Medical Imaging 15 (3)*, pages 278–289, 1996. 1

[13] J. Park, D. Metaxas, and L. Axel. A finite element model for functional analysis of 4d cardiac-tagged mr images. In *Proceedings of Medical Image Computing and Computer-Assisted Intervention*, pages 491–498, 2003. 1

[14] K. Park, D. N. Metaxas, and L. Axel. LV-RV shape modeling based on a blended parameterized model. In *Proceedings of Medical Image Computing and Computer-Assisted Intervention*, pages 753–761. Springer-Verlag, 2002. 1

[15] K. Park, D. N. Metaxas, and L. Axel. A finite element model for functional analysis of 4D cardiac-tagged MR images. In *Proceedings of Medical Image Computing and Computer-Assisted Intervention*, pages 491–498, 2003. 1

[16] Z. Qian, D. N. Metaxas, and L. Axel. Boosting and noparametric based tracking of tagged mri cardiac boundaries. *Proceedings of Medical Image Computing and Computer-Assisted Intervention*, pages 636–644, 2006. 2

[17] M. Teschner, B. Heidelberger, M. Müller, and D. P. M. Gross. Smoothed particles: A new paradigm for animating highly deformable bodies. *Proceeding of Vision, Modeling, Visualization*, pages 47–54, 2003. 3

[18] P. Yan, N. Lin, A. Sinusas, and J. S. Duncan. A boundary element-based approach to analysis of LV deformation. *Proceedings of Medical Image Computing and Computer-Assisted Intervention*, pages 778–785, 2005. 1

[19] A. Young. Model tags: direct 3d tracking of heart wall motion from tagged magnetic resonance images. *Medical Image Analysis*, pages 361–372, 1999. 1